Article

Landsat-7 ETM+, Landsat-8 OLI, and Sentinel-2 MSI Surface Reflectance Cross-Comparison and Harmonization over the Mediterranean Basin Area

Martina Perez * and Marcello Vitale

Posted Date: 20 July 2023

doi: 10.20944/preprints202307.1397.v1

Keywords: Harmonization; Surface Reflectance; Landsat-7; Landsat-8; Sentinel-2; Mediterranean basin

doi:10.20944/preprints202307.1397.v1

Article

Landsat-7 ETM+, Landsat-8 OLI, and Sentinel-2 MSI Surface Reflectance Cross-Comparison and Harmonization over the Mediterranean Basin Area

Martina Perez * and Marcello Vitale

Department of Environmental Biology, Sapienza University of Rome, 00185 Rome, Italy
* Correspondence: martina.perez@uniroma1.it; Tel.: +39-3334155840

Abstract: In the Mediterranean area, vegetation dynamics and phenology analyzed over a long time can have an important role in highlighting changes in land use and cover as well as the effect of climate change. Over the last 30 years, remote sensing has played an essential role in bringing about these changes thanks to many types of observations and techniques. Satellite images are to be considered an important tool to grasp these dynamics and evaluate them in an inexpensive and multidisciplinary way thanks to Landsat and Sentinel satellite constellations. The integration of these tools holds a dual potential: on one hand, allowing to obtain longer historical series of reflectance data, while on the other hand, making data available with a higher frequency even within a specific timeframe. The study aims to conduct a comprehensive cross-comparison analysis of long-time series pixel values in the Mediterranean regions. For this scope comparisons between Landsat-7 (ETM+), Landsat-8 (OLI), and Sentinel-2 (MSI) satellite sensors were conducted based on surface reflectance products. We evaluated these differences using Ordinary Least Squares (OLS) and Major Axis linear regression (RMA) analysis on points extracted from over 15,000 images across the Mediterranean basin area from 2017 to 2020. Minor but consistent differences were noted, necessitating the formulation of suitable adjustment equations to better align Sentinel-2 reflectance values with those of Landsat-7 or Landsat-8. The results of the analysis are compared with the most used harmonization coefficients proposed in the literature, revealing significant differences. The root mean square deviation, the mean difference and the orthogonal distance regression (ODR) slope show an improvement of the parameters for both models used (OLS and RMA) in this study. The discrepancies in reflectance values lead to corresponding variations in the estimation of biophysical parameters, such as NDVI, showing an increase in the ODR slope of 0.3. Despite differences in spatial, spectral, and temporal characteristics, we demonstrate that integration of these datasets is feasible through the application of band-wise regression corrections for a sensitive and heterogeneous area like those of the Mediterranean basin area.

Keywords: harmonization; surface reflectance; Landsat-7; Landsat-8; Sentinel-2; mediterranean basin

---

1. Introduction

Over the past few decades, remote sensing has emerged as a powerful tool with great potential in numerous areas of land monitoring. It plays a crucial role in supporting global efforts in ecology and forest management [1]. The availability of approximately 40 years of free satellite data has transformed the approach to ecological monitoring practices [2].

Remote sensing has a wide range of applications in the field of ecology, utilizing information from satellite constellations such as Landsat, Sentinel, and MODIS. The diverse applications include land cover change/use analysis [3], estimation of fractional vegetation cover [4], crop monitoring [5,6], analysis of forest vegetation health [7–9], biodiversity [10] and soil erosion [11] assessment and monitoring.

The analysis of historical time series of vegetation indices and indicators offer huge potential for investigating temporal dynamics such as land cover change and understanding the impacts of climate change. By studying the changing patterns over time with a hight frequency of data, we can gain valuable insights into the effects of climate change on vegetation and its ecosystems.

Therefore, there is a widespread acknowledgement regarding the significance of investigating prolonged changes in the Earth's land surface and establishing a reliable, uninterrupted series of vegetation index data that accurately captures the fluctuations in vegetation patterns. This is crucial for extracting valuable information about seasonal vegetation characteristics such as green vegetation cover and leaf area index, as well as comprehending interannual variations related to land degradation, forest disturbances, climate changes, and vegetation classification [12–14].

The effects of global climate change on terrestrial ecosystems have been substantial over the last century [15–18]. It is fundamental to explore the spatial and temporal patterns of ecosystem responses to climate change [19].

Given the vast amount of data covering a wide historical range, the use of satellite products is an important opportunity in the field of environmental monitoring.

A combination of Landsat-7, Landsat-8, Sentinel-2A, and Sentinel-2B satellite data can yield a worldwide median average revisit interval of 2.9 days. Over one year, this combination can also provide a median minimum revisit interval of 14 minutes (±1 minute) and a maximum revisit interval of 7.0 days [20].

The potential of these tools becomes particularly relevant when they are compared and integrated. The standardization of the spatial resolution of spectral bands across satellite platforms allows to obtain a greater quantity of data available for those areas or periods of the year in which the image quality is disrupted by atmospheric phenomena (e.g., cloud cover) [21].

Furthermore, the analysis of the effects of climate change is sometimes local and linked to specific breakpoints, making the greater frequency of data important to detect ecosystem responses to climate change effects [22]. A high frequency of data is a limitation in studies of climate change effects and land cover change, especially in particularly heterogeneous areas.

The Mediterranean Basin region is a highly heterogeneous area that is very sensitive to the effects of climate change and anthropogenic activities, such as floods, wildfires, and deforestation [23,24].In particular, Mediterranean landscapes have some peculiar traits that make them unique compared to all other types of environmental and their geographical composition is characterized by high spatiotemporal heterogeneity of vegetation pattern [25]. The nature and complexity of environmental ecosystems in the Mediterranean basin lead to the necessity of robust and integrated analysis to identify the changes in the landscape and applying efficient environmental monitoring.

Several studies have leveraged the opportunity to harmonize satellite products from the Landsat-8 and Sentinel-2 constellations for investigations conducted in the Mediterranean basin region [26–28]. Few studies have integrated data from the Landsat-7 satellite in the Mediterranean basin area, focusing on specific areas [29,30].

In this study, we sampled surface reflectance images from the Landsat-7 ETM+, Landsat-8 OLI and Sentinel-2 MSI. The main objective of this study was to evaluate the differences between Sentinel-2 MSI, Landsat-8 OLI and Landsat-7 ETM+ surface reflectance data, and to propose cross-sensor transformation coefficients using different regression models (OLS and RMA) to facilitate the integration of these data sources for the entire area of Mediterranean basin regions.

This study represents an advancement compared to the existing literature as it aims to harmonize, for the first time, the surface reflectance products of ETM+, OLI, and MSI sensors specifically for the Mediterranean basin region.

We compared pairs of ETM+, OLI, and MSI image observations and developed regression models to describe the relationships between sensor values. The potential of integrating reflectance values for the Mediterranean basin area was verified by applying different metrics of difference between the values of the models used in this study (OLS, RMA) compared to the coefficients reported in the literature. The comparison with harmonization coefficients proposed by Chastain et al. (2019) [31] and those proposed by Claverie et al. (2018) for the Harmonized Landsat-8 and Sentinel-2 (HLS) [32] data set was implemented to assess a site-specific approach for the harmonization procedure.

doi:10.20944/preprints202307.1397.v1

This comparison will highlight the need for focused analyses that consider the unique characteristics and dynamics of the Mediterranean area. The results will be emphasized by calculating the widely used vegetation index, the Normalized Difference Vegetation Index (NDVI).

2. Materials and Methods

The spectral bands of the MSI, OLI and ETM+ sensors were compared by using pairs of images from different sensors captured on the same day or one day different for OLI and ETM+ comparisons, extracting the values of randomly selected points within the Mediterranean basin area. In the following sections are discussed the study area characteristics and the methodological approach used.

2.1. Study Area

In this study we defined the Mediterranean region as roughly spanning the area between 10°W–40°E and 20°N–50°N (Figure 1)[33]. The Mediterranean region includes the territories bordering the Mediterranean Sea and specific sets of biogeographical and bioclimatic characteristics distinguish it. Covering an approximate area of 2 million of km^2 this region is a convergence point for three continents: Europe, Asia, and Africa. The Mediterranean basin is a transition between arid ecosystems located in North Africa and the Near East, and temperate forest ecosystems found in the European mountains. As reported in Köppen-Geiger classification [34], the Mediterranean climate is categorized as a temperate mid-latitude climate with a dry summer season that can be either warm or hot. It is the most extensive among the five regions worldwide that exhibit a Mediterranean-type climate, and the most intricate in terms of geography, encompassing over 40,000 km of rugged coastline that comprises distinct peninsulas and islands [35]. The region hosts a diverse range of plant communities, spanning from Mediterranean evergreen sclerophyllous forests and maquis formations to steppe-like grasslands and coastal dune systems [36]. The Mediterranean Basin shows remarkable landscape heterogeneity, particularly in terms of vegetation, owing to a combination of biogeographic, climatic, and historical factors [37].

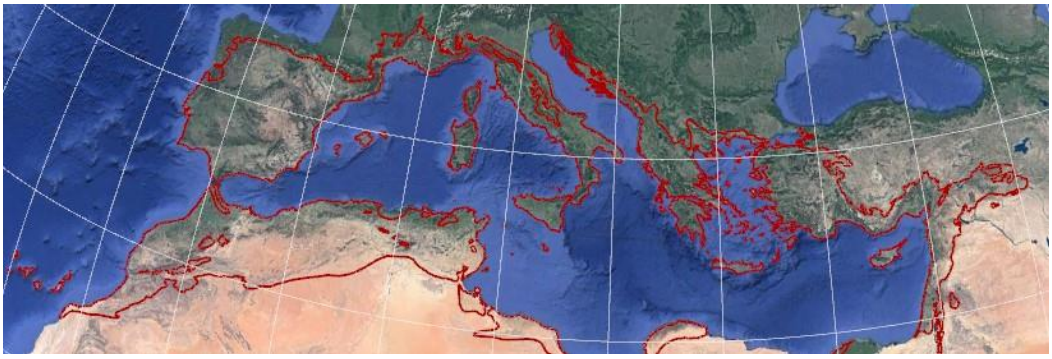

Figure 1. In red the Mediterranean Basin region boundaries. The study area is situated within the Universal Transverse Mercator (UTM) zones ranging from 29 to 37, in white.

2.2. Satellite Data

In this paper, surface reflectance images of the Landsat-7, Landsat-8 and Sentinel-2 over the Mediterranean region were used.

The Landsat-7 satellite carries the Enhanced Thematic Mapper Plus (ETM+) sensor, it was launched on April 15, 1999, and provided scientific information for 23 years until April 6, 2022 [38]. The USGS Landsat-7 surface reflectance (SR) product was used (Landsat-7 level 2 collection 2), this dataset contains atmospherically corrected and orthorectified surface reflectance [39,40]. The Landsat-7 SR dataset was developed with the Landsat Ecosystem Disturbance Adaptive Processing System (LEDAPS) algorithm (version 3.4.0)[41].

The Landsat-8 satellite carries two sensors on board: the Operational Land Imager (OLI) and the Thermal Infrared Sensor (TIRS) and it was launched on February 11, 2013 [42,43]. The USGS Landsat-8 SR dataset (Landsat-8 level 2 collection 2) which contains atmospherically corrected, orthorectified surface reflectance data was used [40]. Landsat-8 SR products are developed with the Land Surface Reflectance Code (*LaSRC*) [32,39,44,45]. Both Landsat-7 and Landsat-8 have a revisit cycle of 16 days.

The Sentinel-2 mission is a constellation of two polar-orbiting satellites that carries a Multispectral Instruments (MSI): once Sentinel-2A launched on June 24, 2015; once Sentinel-2B launched on March 7, 2017 [46]. The combined Sentinel-2 constellation revisit is 5 days. Sentinel-2 MSI surface reflectance data (Sentinel-2, level-2) are generated by the Sen2Cor software [47–49].

SR products were preferred to minimize differences due to atmospheric effects [50]. Despite the visually similar appearance of the data collected by the sensors, they differ in terms of the number of bands, band centre, bandwidth, and spatial resolution (Table 1).

Table 1. The nominal band centres, bandwidths, and spatial resolution of Sentinel-2 MSI, Landsat-8 OLI and Landsat-7 ETM+. The asterisk (*) indicates bands that are not assessed in this study. Source of Landsat-7 ETM+ and Landsat-8 OLI specifications, USGS (https://earthexplorer.usgs.gov/). Sentinel-2 MSI specifications, ESA Copernicus data centre (https://scihub.copernicus.eu/dhus/#/home).

Sentinel-2/MSI													
Band ID	**B1***	**B2**	**B3**	**B4**	**B5***	**B6***	**B7**	**B8**	**B8A**	**B9***	**B10***	**B11**	**B12**
Band centre (nm)	**442.7**	**492.4**	**559.8**	**664.6**	**704.1**	**740**	**782.8**	**832.8**	**864.7**	**1373.5**	**945.1**	**1613.7**	**2202.4**
Nominal bandwidth (nm)	**21**	**66**	**36**	**31**	**15**	**15**	**20**	**106**	**21**	**31**	**20**	**91**	**175**
Spatial resolution (m)	**60**	**10**	**10**	**10**	**20**	**20**	**20**	**10**	**20**	**60**	**60**	**20**	**20**
Landsat-8/OLI													
Band ID	**B1***	**B2**	**B3**	**B4**	**B5**	**B6**	**B7**	**B8***	*NA*	**B9***	**B10***	**B11***	*NA*
Band centre (nm)	**443**	**482.5**	**562.5**	**655**	**865**	**1610**	**2200**	**865**	/	**1375**	**10,895**	**12005**	/
Nominal bandwidth (nm)	**20**	**65**	**75**	**50**	**40**	**100**	**200**	**40**	/	**30**	**590**	**1010**	/
Spatial resolution (m)	**30**	**30**	**30**	**30**	**30**	**30**	**30**	**15**	/	**30**	**100**	**100**	/
Landsat-7/ETM+													
Band ID	**B1**	**B2**	**B3**	**B4**	**B5**	**B6***	**B7**	**B8***	*NA*	*NA*	*NA*	*NA*	*NA*
Band centre (nm)	**485**	**560**	**660**	**835**	**1650**	**11,450**	**2220**	**710**	/	/	/	/	/
Nominal bandwidth (nm)	**70**	**80**	**60**	**130**	**200**	**2100**	**260**	**380**	/	/	/	/	/
Spatial resolution (m)	**30**	**30**	**30**	**30**	**30**	**60**	**30**	**15**	/	/	/	/	/

Our study was based on the six common bands among the sensors: blue, green, red, near infrared (NIR), shortwave-infrared 1 (SWIR1) and shortwave-infrared 2 (SWIR2) (Table 2). In this paper, we will refer satellites by using the names of their respective sensors.

Table 2. Nominal spectral band and corresponding band numbers for each sensor. The wavelength range (nm) are included in parentheses.

Spectral band	*Sentinel-2*	*Landsat-8*	*Landsat-7*
Blue	2 (458–522nm)	2 (450–510nm)	1 (450–520nm)
Green	3 (543–578nm)	3 (530–590nm)	2 (520–600nm)
Red	4 (650–680nm)	4 (640–670nm)	3 (630–690nm)
Near Infra-Red (NIR)	8 (785–900nm) 8A (855-875nm)	5 (850–880nm)	4 (770–900nm)
Short Wave Infra-Red 1 (SWIR1)	11 (1565–1655nm)	6 (1570–1650nm)	5 (1550–1750nm)
Short Wave Infra-Red 2 (SWIR2)	12 (2100–2280nm)	7 (2110–2290nm)	7 (2090–2350nm)

2.3. Data Processing and Sampling Design

The surface reflectance images were sampled from MSI, OLI and ETM+ sensors lasting from 2017 to 2021. This specific time range was chosen as it represents the last full calendar years in which complete image collections for all three sensors were fully available at the time of the study.

Clouds and cloud shadows can affect the spectral bands and distort their results. Masking was performed using the *CFmask* algorithm [51,52] for ETM+ and OLI products. The quality assessment band (QA60) in the metadata of Sentinel-2 was used to detect and mask clouds and cloud shadows. The cloudy pixel percentage permitted was less than 20% to minimize cloud and cloud shadow effects.

To facilitate a project that produces 30 m spatial resolution outputs, the last processing step entailed reprojecting all image pairs to the projection and 30-meter grid of the initial Landsat OLI image (WGS 84, UTM Zone n - where n denotes the zone number associated with the corresponding Landsat OLI image). To adjust the 10 m and 20 m MSI bands to a 30 m spatial resolution, bicubic interpolation was selected over bilinear or nearest-neighbour interpolation due to its ability to yield a smoother surface. A total of 1500 georeferenced random points were generated within the Mediterranean basin area to sample the entire range of potential spectral values in the area. The available ETM+, OLI, and MSI values between 2017 and 2021 were extracted for each of these points.

The distinct orbits and swath widths of OLI/ETM+ and MSI sensors facilitate the identification of numerous instances where both satellites capture the same ground locations on the same day. For OLI and ETM+ there are not same-day instances, but instances of 1-day lag were sampled. It is reasonable to assume that there are no significant changes in land surface and atmospheric conditions between the two acquisitions on the same day or adjacent day. Since both satellites are sun-synchronous and have mid-morning overpass time, the pairs of observations are generally only minutes apart, and it can be inferred that no significant changes in land surface occur between the two observations, as demonstrated by Flood (2017)[53].

The pixel values intersecting the sample point location were extracted for the blue, green, red, NIR, SWIR1, and SWIR2 bands for each platform-sensor pair.

All data extraction was carried out by Google Earth Engine (GEE), a catalogue of satellite imagery and geospatial datasets spanning multiple petabytes with the ability to perform planetary-scale analysis. GEE integrates with a high-performance computation service and is accessed through an Internet-accessible application programming interface (API) in JavaScript coding, enabling efficient data analysis and rapid visualization of results [40].

To remove any remaining undetected cloud or shadow, the blue band ratio between two sensors (MSI vs OLI, MSI vs ETM+, OLI vs ETM+) was computed. Any data points exhibiting a ratio greater than 2 or less than 0.5 were excluded, on the assumption that these pixels were corresponding to areas that were cloud-free in one image but appeared brighter due to cloud presence or darker due to shadowing in the other image [53]. Following a procedure similar to that reported in [31], all outlier values beyond four standard deviations were checked and removed (Table 3)

Table 3. Sample points numbers of each pairwise comparison.

Sensor	*Sample Points*
MSI vs OLI	35234
MSI vs ETM+	25880
OLI vs ETM+	25640

2.4. Method of Analysis

In this study, all sample observations were split into a training (70%) and test (30%) dataset of pairwise pixels (Table 4).

Table 4. Sample points numbers of each pairwise comparison split into a training and test set.

	Training Set	*Test Set*
MSI vs OLI	24664	10570
MSI vs ETM+	18116	7764
OLI vs ETM+	17948	7692

Scatterplots were computed to visualize the comparison, where the x-axis stood for the pixel values of Sentinel-2 or Landsat-8, and the y-axis represented the pixel values of Landsat-7 or Landsat-8.

Each scatterplot also displayed the slope of the Orthogonal Distance Regression (ODR) that shows the linear relationship value considering errors in both the independent and dependent variables. The ODR slope measures the change in the dependent variable (e.g., pixel values) for a unit change in the independent variable (e.g., another set of pixel values) in a regression model.

The ODR (Orthogonal Distance Regression) slope closer to one suggests that the two sets of pixel values have a direct, proportional relationship, where an increase or decrease in one set corresponds to an equal increase or decrease in the other set. it indicates a stronger and more consistent linear relationship between the pixel values.

Finally, the resulting regression model was applied to adjust the band values of the training and test set.

Two regression model types were computed: Ordinary Least Squares (*OLS*) and Major Axis (*RMA*) regression models.

OLS regression models were used to assess difference between different bands for the respective sensors. To fit prediction models the equation (1) was fitted for each band:

$$p_x = a + bp_x \tag{1}$$

where p_x is the surface reflectance for Landsat 7/8 and Sentinel-2 at a given wavelength, based on the training set pairwise and parameters a and b are intercept and slope applicable to each band, respectively.

RMA regression model, used in [31] was also employed to determine the value of differences between the sensors. Unlike OLS models, RMA assumes that both the dependent and independent variables can be subject to error [54]. This analysis was implemented using the '*maregress*' function available in MATLAB (https://www.mathworks.com/matlabcentral/fileexchange/27916-maregress).

A *t*-test was used with a significance *p-value* < 0.05 to assess the relationship between pairs of band reflectance values and determine the accuracy of regression model coefficients. Additionally, two metrics of difference were utilized: the mean difference (Δ) and the root mean square deviation (RMSD). The mean difference metric (eq.2) provided insights into the average deviation between the predicted and observed reflectance values, indicating systematic bias in the regression model. The mean difference represents the arithmetic average of the individual differences between paired values, capturing the overall directional discrepancy.

$$\Delta = \sum_{i}^{n} \frac{(v_i^a - w_i^b)}{n} \tag{2}$$

RMSD is a statistical measure commonly used in data analysis and computational modelling to quantify the discrepancy or difference between two distributions of data points. It provides a robust estimate of the average deviation or dispersion between corresponding data points, from the two distributions (v_i^a) and (w_i^b) respectively (eq.3).

$$RMSD = \sqrt{\frac{1}{N}\sum_{i}^{n} * (v_i^a - w_i^b)^2} \tag{3}$$

where v_i^a and w_i^b vary following the relationship investigated (MSI vs OLI, MSI vs ETM+, OLI vs ETM+).

In the last step, the coefficients obtained for data harmonization were compared with those proposed in [32] for the NASA HLS product and in [31] for the CONUS area.

At the time of writing the paper, no harmonization coefficients between the MSI and ETM+ sensors have been released for the NASA HLS product.

The Normalized Difference Vegetation Index (NDVI) for the test dataset pairwise was calculated at aiming to compare the reflectance's value and assess the effectiveness of the correction. It is computed by normalizing the difference between near-infrared and red spectral reflectance for both, harmonized and not harmonized data. Moreover, NDVI was calculated by using both uncorrected and corrected reflectance values obtained from the OLS and RMA regression models.

3. Results

The results of the conducted analyses will be presented to highlight the differences and similarities among the various pairs of sensor surface reflectance values. To better appreciate the differences observed before and after applying the adjusted coefficients, the values related to the analyses conducted on the training sets will be reported in the text. These analyses were confirmed and implemented on the test sets, as demonstrated by the results reported in the supplementary materials (Supplementary materials, Tables S1–S6).

3.1. MSI vs OLI

Regarding the comparison of surface reflectance between resampled MSI and OLI pixel values a reference scatterplot was observed using the training dataset (70%) (Figure 2).

The values exhibit a good level of agreement, as indicated by the dashed line representing the ODR slope, whose values (Table 5) are close to 1. The blue band has a higher degree of disagreement (0.8284). Nevertheless, the mean difference values for all bands (Table 5) are statistically significant (*p-value* < 0.05). The RMSD values (Table 2) range from 0.0197 (Green band) to 0.0464 (SWIR2 band).

Table 5. Statistical differences in surface reflectance between the MSI and OLI band value. ODR slope, mean difference, and RMSD values for each pairwise band of the training set, including a total of 24,664 data points. The asterisk (*) indicates the significance of the *t*-test, with *a p-value* < 0.05.

Band	***ODR Slope***	***Mean Difference***	***RMSD***
Blue	0.8284	0.0115*	0.0206
Green	0.9158	0.0074*	0.0197
Red	0.9064	0.0122*	0.0272
NIR	0.9586	0.0025*	0.0368

NIRa	0.9563	0.0108*	0.0379
SWIR1	0.9484	0.0246*	0.0451
SWIR2	0.8958	0.0307*	0.0464

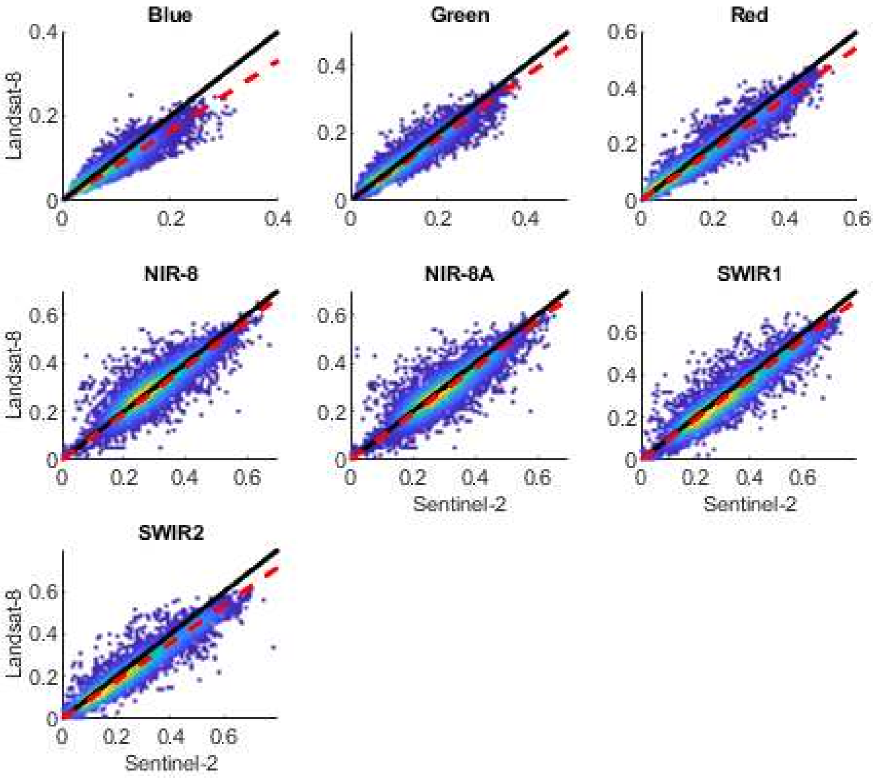

Figure 2. Comparison of pairwise surface reflectance from Sentinel-2 and Landsat-8. In yellow the regions that represents larger numbers of points. The solid line is 1-to-1 relationship, dashed line is the ODR regression slope.

Significant differences have been identified when adjustment factors found here (Table 6) were compared with those available in the literature in [31,32] (Table 7).

Table 6. Intercept and slope values obtained by applying both OLS and RMA regression models for each pair of MSI surface reflectance as a function of OLI surface reflectance.

Regression model	*Blue*	*Green*	*Red*	*NIR*	*NIRa*	*SWIR1*	*SWIR2*
OLS Intercept	0.0016	0.0009	-0.0005	0.0133	0.0204	0.02	0.0113
OLS Slope	1.1297	1.0518	1.0773	0.9637	0.9677	1.0147	1.0829
RMA Intercept	-0.0044	0.0041	0.0047	0.0103	-0.0028	0.0077	0.0035
RMA Slope	1.2071	1.0919	1.1032	1.0432	1.0457	1.0544	1.1163

Table 7. Statistical differences in surface reflectance between the training set MSI and OLI band value after transformation function. Mean difference (a) and RMSD values (b) for each pairwise band of the training set subjected to OLS and RMA regression model in this study, [31] and HLS [32] transformation function The asterisk (*) indicates the significance of the t-test, with a *p-value* < 0.05. "NA" indicates the absence of a transformation coefficient between band 8 and band 5 of the MSI and OLI sensors respectively.

a)			**Mean Difference MSI vs OLI adjusted**	
Band	**OLS**	**RMA**	**Chastain et al. Coeff.**	**HLS Coeff.**
Blue	-2.54E-05	2.67E-05	0.015*	0.0055*
Green	2.78E-05	6.69E-06	0.0043*	0.0071*
Red	1.73E-05	-9.42E-03*	0.0051*	0.0104*
NIR	4.81E-05	-2.06E-02*	0.0304*	*NA*
NIRa	-8.24E-03	-8.27E-03	-0.0038*	0.0026*
SWIR1	8.04E-07	1.06E-06	0.0165*	0.0247*
SWIR2	-8.20E-02*	4.74E-06	0.0261*	0.0288*
b)			**RMSD MSI vs OLI adjusted**	
Band	**OLS**	**RMA**	**Chastain et al. Coeff.**	**HLS Coeff.**
Blue	0.0162	0.0165	0.0221	0.0177
Green	0.018	0.0182	0.0187	0.0197
Red	0.023	0.025	0.0237	0.026
NIR	0.0366	0.0426	0.048	*NA*
NIRa	0.0375	0.0383	0.0372	0.0368
SWIR1	0.0378	0.0382	0.0413	0.0452
SWIR2	0.0938	0.0333	0.0434	0.045

The coefficients available in the literature and applied to our dataset revealed statistically significant differences (*p-value* <0.05) (Table 7a) for all comparisons between MSI and OLI bands adjusted, with RMSD values (Table 7b) ranging from 0.0187 (green band) to 0.0480 (NIR band) for Chastain et al. (2019) [31] transformation functions, and RMSD values ranging from 0.0177 (blue band) to 0.0452 (SWIR1 band) for the HSL [32] transformation functions.

The regression models developed in this study (OLS and RMA) both improved the fitting of the data for all band pairs (Table 7). The OLS model showed a statistically significant difference only in the SWIR2 band, with RMSD values of 0.0375 and 0.0938, respectively, and a *p-value* of 2.20E-16. The RMA transformation function showed a statistically significant difference (Table 7a) in the red band (RMSD 0.0250), NIR band (RMSD 0.0426), (Table 7b), with an average *p-value* of 4.27E-21. Although some difference values were not significant, an improvement can be observed compared to the initial RMSD values (Table 5). Similarly, for these values, the ODR slope is much closer to the 1-to-1 line (Table 8).

Table 8. ODR slope values of MSI and OLI comparison after transformation function application**.**

MSI vs OLI ODR Adjusted		
Band	**OLS**	**RMA**
Blue	0.9424	1.0108
Green	0.9649	1.0030
Red	0.9781	1.0021
NIR	0.9211	1.0034
NIRa	0.9231	1.0035
SWIR1	0.9629	1.0020
SWIR2	1.0262	1.0031

doi:10.20944/preprints202307.1397.v1

3.2. *MSI vs ETM+*

The scatterplot representing the comparison between paired surface reflectance values of satellites Sentinel-2 and Landsat-7 pixel (training dataset) was reported in Figure 3. This comparison between sensors also demonstrates a good level of agreement, as evidenced by the dashed line representing the ODR slope values (Figure 3; Table 9).

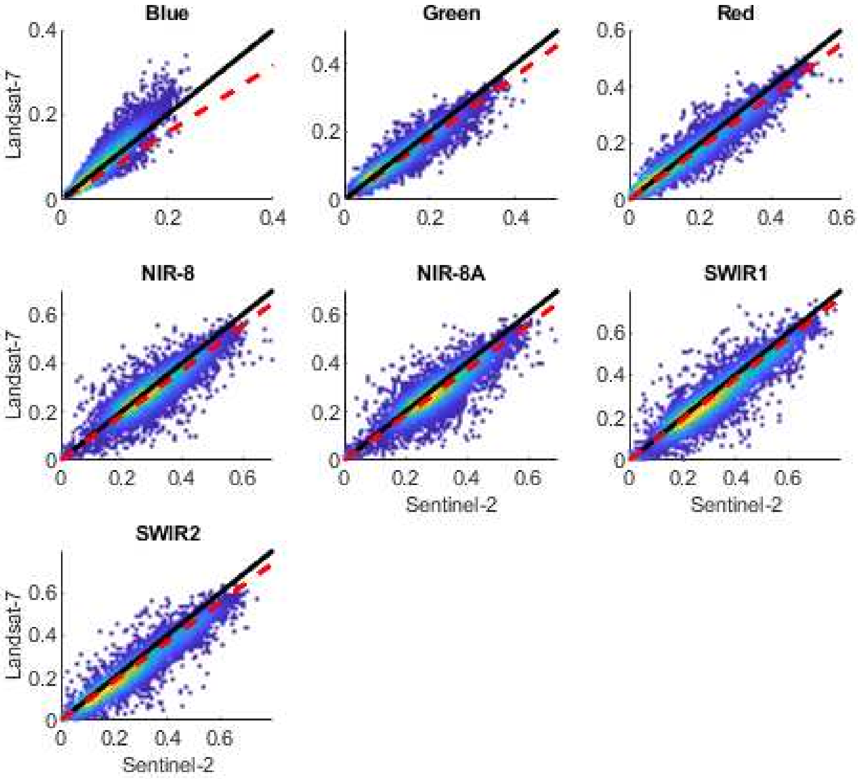

Figure 3. Comparison of pairwise surface reflectance from Sentinel-2 and Landsat-7. In yellow are regions that represents larger numbers of points. The solid line is 1-to-1 relationship, dashed line is the ODR regression slope**.**

The blue band has a higher degree of disagreement (ODR slope, 0.7901).

Table 9. Statistical differences in surface reflectance between the MSI and ETM+ band value. ODR slope, mean difference, and RMSD values for each pairwise band of the training set, comprising a total of 18,116 data points. The asterisk (*) indicates the significance of the t-test, with a *p-value* < 0.05.

Band	*ODR slope*	*Mean difference*	*RMSD*
Blue	0.7901	0.0065*	0.0196
Green	0.9119	0.0055*	0.0210
Red	0.9164	0.0083*	0.0274
NIR	0.9243	0.0156*	0.0422
NIRa	0.9238	0.0232*	0.0457
SWIR1	0.9564	0.0273*	0.0505
SWIR2	0.9251	0.0329*	0.0498

Nevertheless, the mean difference values for all bands comparison are statistically significant (*p-value* < 0.05) and the RMSD values range from 0.0196 (Blue band) to 0.0505 (SWIR1 band) (Table 9).

Appling adjustment coefficients of the regression models from this study (OLS/RMA) (Table 10) and those available in the literature [31] statistical difference were appreciated (Table 11).

Table 10. Intercept and slope values obtained by applying both OLS and RMA regression models for each pair of MSI surface reflectance as a function of ETM+ surface reflectance.

Regression model	*Blue*	*Green*	*Red*	*NIR*	*NIRa*	*SWIR1*	*SWIR2*
OLS Intercept	-0.0083	-0.0037	-0.0041	0.0065	0.0038	0.0067	-0.0083
OLS Slope	0.9375	0.934	0.9325	0.959	0.9416	0.9246	0.9375
RMA Intercept	-0.0119	-0.0067	-0.0067	-0.0063	-0.0054	0.0010	-0.0119
RMA Slope	0.9764	0.9554	0.9464	1.0009	0.9688	0.9462	0.9764

The coefficients available in the literature and applied to our dataset revealed statistically significant differences (*p-value* <0.05) (Table 11a) for all comparisons between MSI and ETM+ bands adjusted, except for the red band. RMSD values (Table 11b) range from 0.0026 (green band) to 0.0449 (NIR band) for [31] transformation functions.

The regression models developed in this study (OLS and RMA) both improved the fitting of the data for all band pairs (Table 11). No statistically significant difference was revealed by the t-test *p-value*. An improvement can be observed compared to the initial RMSD values (Table 9) and post-transformation RMSD values those range from 0.0172 (blue band) to 0.0425 (SWIR1 band), and from 0.0176 (blue band) to 0.0430 (SWIR1 band) following the OLS and RMA transformation function, respectively.

Table 11. Statistical differences in surface reflectance between the MSI and ETM+ band value after transformation function. Mean difference (a) and RMSD values (b) for each pairwise band of the training set subjected to OLS and RMA regression model in this study and to Chastain et al. (2019) [31] transformation function. The asterisk (*) indicates the significance of the t-test, with a *p-value* < 0.05.

a)	**Mean Difference MSI vs ETM+ adjusted**		
Band	**OLS**	**RMA**	**Chastain et al. Coeff.**
Blue	*-7.68E-06*	4.40E-05	0.0116*
Green	*1.91E-06*	4.54E-05	0.0026*
Red	*4.62E-06*	-1.05E-05	0.001
NIR	*3.68E-05*	-1.24E-05	0.0219*
NIRa	*-5.09E-05*	-1.40E-05	-0.006*
SWIR1	*6.16E-05*	4.80E-05	0.0121*
SWIR2	*3.66E-05*	-3.22E-05	0.0149*
b)	**RMSD MSI vs ETM+ adjusted**		
Band	**OLS**	**RMA**	**Chastain et al. Coeff.**
Blue	***0.0172***	0.0176	0.0209
Green	***0.0201***	0.0204	0.0206
Red	***0.0253***	0.0255	0.0253
NIR	***0.0392***	0.0401	0.0449
NIRa	***0.0394***	0.0404	0.0426
SWIR1	***0.0425***	0.043	0.0445
SWIR2	***0.0369***	0.0373	0.0398

At the same time, the post-transformed ODR slope is much closer to the 1-to-1 line (Table 12) with respect to the initial value (Table 9).

Table 12. ODR slope values of MSI and ETM+ comparison after transformation function application.

MSI vs ETM+ ODR adjusted		
Band	**OLS**	**RMA**
Blue	0.9339	1.0155
Green	0.9555	1.0041
Red	0.9734	1.0023
NIR	0.9134	1.0068
NIRa	0.9124	1.0070
SWIR1	0.9542	1.0020
SWIR2	0.9658	1.0026

3.3. *OLI vs ETM+*

The scatterplot standing for the comparison between paired surface reflectance values of satellites Landsat-8 and Landsat-7 pixel (training dataset) was reported in Figure 4. This inter-comparison between sensors has the best grade of agreement, as evidenced by the dashed line representing the ODR slope values which - in some cases - coincides with the 1-to-1 line (Blue band) (Figure 4; Table 13). The NIR band has the higher degree of disagreement (0.9992).

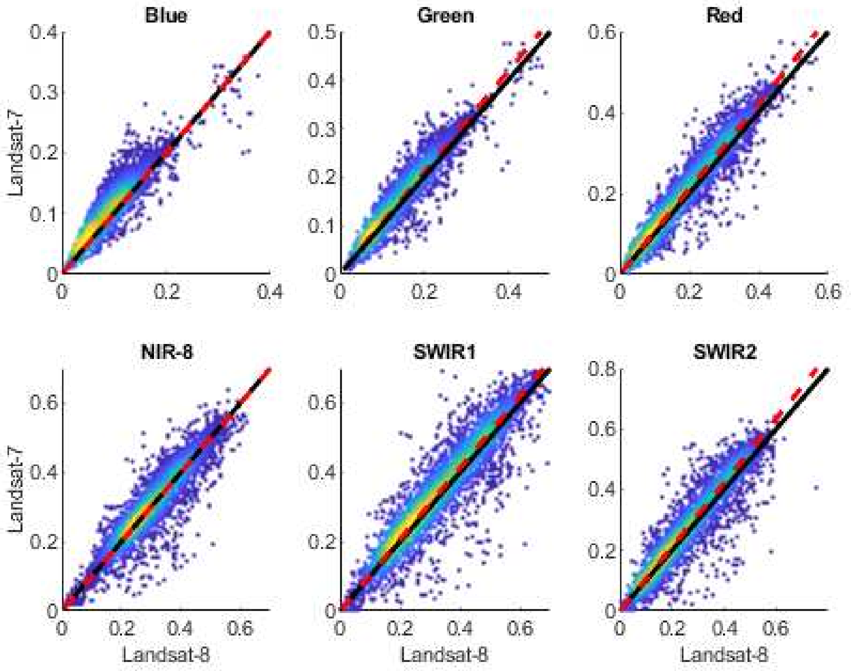

Figure 4. Comparison of pairwise surface reflectance from Landsat-8 and Landsat-7. In yellow are the regions that represents larger numbers of points. The solid line is 1-to-1 relationship, dashed line is the ODR regression slope.

Table 13. Statistical differences in surface reflectance between the OLI and ETM+ band value. ODR slope, mean difference, and RMSD values for each pairwise band of the training set, comprising a total of 25,640 data points. The asterisk (*) indicates the significance of the t-test, with a *p-value* < 0.05.

Band	*ODR slope*	*Mean difference*	*RMSD*
Blue	1.0026	-0.0141*	0.0186
Green	1.0467	-0.0131*	0.0196
Red	1.0566	-0.0169*	0.0256
NIR	0.9992	-0.0060*	0.0267
SWIR1	1.0322	-0.0159*	0.0366
SWIR2	1.0569	-0.0130*	0.0327

The mean difference values for all bands comparison (Table 13) are statistically significant (*p-value* < 0.05). The RMSD values range from 0.0186 (Blue band) to 0.0366 (SWIR1 band).

Statistical difference was observed applying adjustment coefficients of the regression models from this study (OLS/RMA) (Table 14) and those available in the literature [31].

Table 14. Intercept and slope values obtained by applying both OLS and RMA regression models for each pair of OLI surface reflectance as a function of ETM+ surface reflectance.

Regression model	*Blue*	*Green*	*Red*	*NIR*	*SWIR1*	*SWIR2*
OLS Intercept	-0.0083	-0.0037	-0.0041	0.0065	0.0038	0.0067
OLS Slope	0.9375	0.934	0.9325	0.959	0.9416	0.9246
RMA Intercept	-0.0119	-0.0067	-0.0067	-0.0063	-0.0054	0.0010
RMA Slope	0.9764	0.9554	0.9464	1.0009	0.9688	0.9462

The coefficients available in the literature and applied to our dataset revealed statistically significant differences (*p-value* <0.05) (Table 15a) for all comparisons between MSI and ETM+ bands adjusted, RMSD ranging from 0.0173 (green band) to 0.0442 (SWIR2 band) for Chastain et al. (2019) [31] transformation functions (Table 15b).

The regression models developed in this study (OLS and RMA) both improved the fitting of the data for all band pairs (Table 15). No statistically significant difference was revealed by the t-test *p-value*. An improvement can be observed compared to the initial RMSD values (Table 13) and post-transformation RMSD values. The RMSD range is very similar to the results obtained from the transformation coefficients application of both regression models (OLS, RMA). The RMSD ranges from 0.12 for the blue band to 0.028 for the SWIR2 band. The ODR slope post-transformation function is much closer to the 1-to-1 line (Table 12).

Table 15. Statistical differences in surface reflectance between the OLI and ETM+ band value after transformation function. Mean difference (a) and RMSD values (b) for each pairwise band of the training set subjected to OLS and RMA regression model in this study and to the Chastain et al. (2019) [31] transformation function. The asterisk (*) indicates the significance of the t-test, with a *p-value* < 0.05.

a)	**Mean Difference OLI vs ETM+ adjusted**		
Band	**OLS**	**RMA**	**Chastain et al. Coeff.**
Blue	1.06E-07	4.88E-06	-0.0118*
Green	-5.29E-07	-3.68E-05	-0.0136*
Red	3.49E-05	-4.85E-06	-0.0186*
NIR	-1.80E-05	1.49E-05	-0.0326*
SWIR1	-5.56E-05	3.79E-06	-0.026*
SWIR2	-3.72E-05	4.33E-05	-0.0293*
b)	**RMSD OLI vs ETM+ adjusted**		
Band	**OLS**	**RMA**	**Chastain et al. Coeff.**
Blue	0.0119	0.012	0.0173
Green	0.0139	0.0139	0.02
Red	0.0179	0.0179	0.0274
NIR	0.0258	0.026	0.0446
SWIR1	0.0319	0.0321	0.0435
SWIR2	0.0282	0.0284	0.0442

The post-transformed ODR slope values have not shown significant changes, as the original values were already very close to the 1-to-1 line (Appendix, Table A1)

3.4. NDVI Computation

Figure 5 presents a comparison between NDVI computed from MSI and OLI sensors on the test set (10,570 pairwise samples). Specifically, it is reported the comparison between the sensor value pairs before applying adjustment coefficients. The orthogonal distance regression (ODR) slope is measured at 0.92, and the mean difference with a value of -0.0243 shows statistical significance (t-test, *p-value* 1.63E-14). Additionally, the Root Mean Square Deviation (RMSD) is computed to be 0.050 (Figure 5a).

The same comparison is made after applying the adjustment factors from the OLS model in Table 6 (Fig.5b). The ODR slope has increased to 0.95, and the mean difference, with a value of -0.0211, is no longer statistically significant (t-test, *p-value* 0.7204). The RMSD remains unchanged. The comparison with Landsat-7 is omitted for brevity; however, it exhibits very similar behaviour to the previous comparisons.

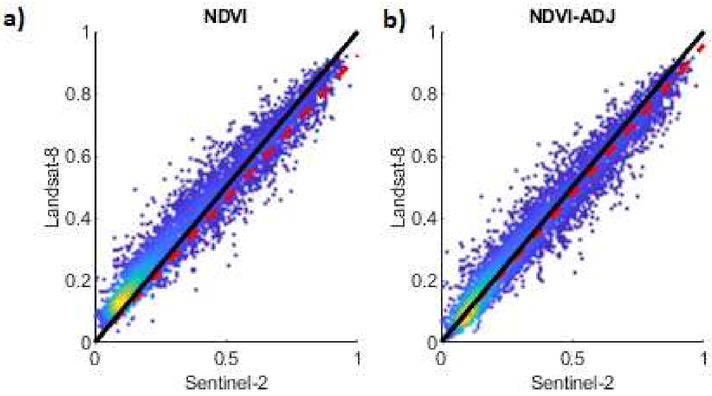

Figure 5. Comparison of NDVI from Sentinel 2 and Landsat-8 from test dataset; (**a**) with uncorrected surface reflectance; (**b**) with adjusted OLS factor (Table 6). In yellow are the regions that represents larger numbers of points. The solid line is 1-to-1, dashed line is the ODR regression slope.

4. Discussion

This study aims to assess the differences and propose cross-sensor conversion factors derived from the integrated or exclusive use of OLS and RMA regression models between Landsat-7, Landsat-8, and Sentinel-2 surface reflectance products. The objective is to take advantage of the potential arising from the harmonization of these products. While previous literature has primarily focused on integrating TOA reflectance products in different areas, this study, for the first time, concentrates on the highly heterogeneous Mediterranean Basin using surface reflectance products, representing a significant advancement in the integration of satellite products within this region.

Despite the good agreement observed in the comparison (Figures 2 and 3) between Landsat-7/8 and Sentinel-2 products, significant variations exist between cross-sensors band pairs, as demonstrated by mean differences and RMSD (Tables 5, 9 and 13). The slope of the ODR shows equivalent results for MSI vs OLI (Table 5) and MSI vs ETM+ (Table 9) comparisons, with values close to 1 for the visible bands, particularly the blue band. A higher disagreement was observed for the blue band between the MSI vs ETM+ sensor pairs where a notable mismatched band width was reported (Table 2). In the case of the NIR band, MSI bands 8 and 8a exhibit remarkably similar ODR slopes and RMSD values when compared to OLI and ETM+ bands 5 and 4, respectively. For the comparison between Landsat 7/8 and Sentinel-1 the greatest deviation (RMSD) is observed in the SWIR bands. The SWIR1 (wavelength range 1565–1655nm) and SWIR2 (wavelength range) bands of MSI exhibit greater deviation compared to the SWIR bands of ETM+ (SWIR1: wavelength range 1570–1750nm, SWIR2: wavelength range 2090–2350nm) respect to the OLI ones (SWIR1: wavelength range

doi:10.20944/preprints202307.1397.v1

1570–1650nm, SWIR2: wavelength range 2110–2290nm). Overall, the RMSD resulting from the MSI vs ETM+ comparison is higher than the RMSD of MSI vs OLI.

As expected, the comparison between sensors from the same satellite family (OLI vs ETM+) shows a higher degree of agreement, as confirmed by the ODR slope, which is still close to 1 (Table 13). In this case as well, the greatest RMSD is observed in the SWIR bands, despite slight differences in the wavelength range (Table 2). Our analysis suggests that all three sensors can be used after calibration and harmonization.

This study presents the results of two regression models, OLS, and RMA, suggesting a mixed band adjustment based on the coefficients of both models and supported by statistical analyses. Taking into consideration the RMSD, the mean difference and the ODR slope values, integrating the coefficients of the two models is suggested for band adjustment. For the harmonization between OLI and MSI bands was suggested the integrating use of RMA coefficients for Blue, Green, NIRa, SWIR1 and SWIR2 bands, and OLS coefficients for Red and NIR bands. For the harmonization between ETM+ and MSI bands was suggested the integrating use of RMA coefficients for Blue and SWIR1 bands, and OLS coefficients for Red, NIR, Green, NIRa and SWIR2 bands. Finally for the harmonization between ETM+ and OLI bands was suggested the integrating use of RMA coefficients for Red, NIR and SWIR2 bands, and OLS coefficients for Blue, Green and SWIR1 bands. However, this approach is not mandatory, as shown in results tables (Tables 7, 11, 15), where both models improve sensor calibration. Application of the proposed coefficients significantly enhances the agreement between sensors, as demonstrated by the calculation of NDVI. The NDVI comparison obtained after band correction proposed shows a slightly improving in mean difference value. It is important to underline that following the adjustment, the difference between the variables decreased to such an extent that it was not statistically significant. Finally, the ODR analysis shows a better agreement between the variables, although the RMSD does not significantly change its value. This observation could be attributed to the NDVI equation, it is obtained from the normalized difference between NIR and RED bands, which does not exhibit a higher degree of disagreement between sensor pairs. It is expected that more complex indices, incorporating other spectral bands, may reinforce these findings. The use of coefficients for sensor calibration is strongly recommended, not only for long-term historical analysis but also to increase data frequency, which is crucial in land cover change analyses, and to overcome issues caused by clouds and shadows [21] . Comparison with coefficients from existing literature highlights the importance of site-specific models [53,55,56]. The difference between the results obtained using the coefficients in this study and those from the literature could be attributed to the sampling method. Claverie et al. (2018) [32] work for the HLS product was based on a global dataset with few sampled points in the Mediterranean Basin, while Chastain et al. (2019) [31] proposed a method based on points sampled in the CONUS region. Another explanation could be attributed to different techniques for transforming surface reflectance, which is why the authors of this study chose to utilize a pre-existing surface reflectance product to avoid such issues for users [57].

5. Conclusions

The results obtained from this study aim to provide a harmonization procedure that allows for expanding the availability of comparable surface reflectance data for the Mediterranean basin area. The analysis of surface reflectance products demonstrates a good level of agreement, but the conducted analyses and comparisons with existing studies in the literature have highlighted the potential of integrating the available products with site-specific transformation factors.

The use of a high number of random points (1500) sampled in the Mediterranean region and evaluating the model performance on a training set (70%) and a test set (30%), stated that the coefficients reported in this study can be used to harmonize the spectral bands of ETM+, OLI, and MSI surface reflectance products for landscape studies in the Mediterranean Basin area. Satellite data processing was conducted using open-source software (GEE) and freely accessible surface reflectance datasets. This ensures the reproducibility of the methodological approach and enables its widespread application to other study areas.

The authors did not apply BRDF and haze corrections since the aim of the study was to develop band-wise correction factors applicable to a broad range of users. It is assumed that the application of such corrections could further enhance the results already obtained in this study. The future challenge will undoubtedly involve integrating these corrections into the proposed model and assessing their contribution.

Supplementary Materials: the following supporting information can be downloaded at : www.mdpi.com/xxx/s1, APPENDIX A (Table A.1 – a.6) , APPENDIX B (Table B.1).

Author Contributions: Conceptualization: methodology, data, curation, validation, original draft preparation, M.P. Writing-review, supervision, M.V.

Funding: This research received no external funding.

Data Availability Statement: Data and scripts will be made available on request.

Conflicts of Interest: The authors declare no conflict of interest.

References

1. Lechner, A.M.; Foody, G.M.; Boyd, D.S. Applications in Remote Sensing to Forest Ecology and Management. One Earth 2020, 2, 405–412, doi:10.1016/j.oneear.2020.05.001.
2. Wulder, M.A.; Masek, J.G.; Cohen, W.B.; Loveland, T.R.; Woodcock, C.E. Opening the Archive: How Free Data Has Enabled the Science and Monitoring Promise of Landsat. Remote Sens. Environ. 2012, 122, 2–10, doi:10.1016/j.rse.2012.01.010.
3. Gómez, C.; White, J.C.; Wulder, M.A. Optical Remotely Sensed Time Series Data for Land Cover Classification: A Review. ISPRS J. Photogramm. Remote Sens. 2016, 116, 55–72, doi:10.1016/j.isprsjprs.2016.03.008.
4. Gao, L.; Wang, X.; Johnson, B.A.; Tian, Lechner, A.M.; Foody, G.M.; Boyd, D.S. Applications in Remote Sensing to Forest Ecology and Management. One Earth 2020, 2, 405–412, doi:10.1016/j.oneear.2020.05.001.
5. Wulder, M.A.; Masek, J.G.; Cohen, W.B.; Loveland, T.R.; Woodcock, C.E. Opening the Archive: How Free Data Has Enabled the Science and Monitoring Promise of Landsat. Remote Sens. Environ. 2012, 122, 2–10, doi:10.1016/j.rse.2012.01.010.
6. Gómez, C.; White, J.C.; Wulder, M.A. Optical Remotely Sensed Time Series Data for Land Cover Classification: A Review. ISPRS J. Photogramm. Remote Sens. 2016, 116, 55–72, doi:10.1016/j.isprsjprs.2016.03.008.
7. Gao, L.; Wang, X.; Johnson, B.A.; Tian, Q.; Wang, Y.; Verrelst, J.; Mu, X.; Gu, X. Remote Sensing Algorithms for Estimation of Fractional Vegetation Cover Using Pure Vegetation Index Values: A Review. ISPRS J. Photogramm. Remote Sens. 2020, 159, 364–377, doi:10.1016/j.isprsjprs.2019.11.018.
8. Segarra, J.; Buchaillot, M.L.; Araus, J.L.; Kefauver, S.C. Remote Sensing for Precision Agriculture: Sentinel-2 Improved Features and Applications. Agronomy 2020, 10, 641, doi:10.3390/agronomy10050641.
9. Omia, E.; Bae, H.; Park, E.; Kim, M.S.; Baek, I.; Kabenge, I.; Cho, B.-K. Remote Sensing in Field Crop Monitoring: A Comprehensive Review of Sensor Systems, Data Analyses and Recent Advances. Remote Sens. 2023, 15, 354, doi:10.3390/rs15020354.
10. Majasalmi, T.; Rautiainen, M. The Potential of Sentinel-2 Data for Estimating Biophysical Variables in a Boreal Forest: A Simulation Study. Remote Sens. Lett. 2016, 7, 427–436, doi:10.1080/2150704X.2016.1149251.
11. Banskota, A.; Kayastha, N.; Falkowski, M.J.; Wulder, M.A.; Froese, R.E.; White, J.C. Forest Monitoring Using Landsat Time Series Data: A Review. Can. J. Remote Sens. 2014, 40, 362–384, doi:10.1080/07038992.2014.987376.
12. Wang, L.; Jia, M.; Yin, D.; Tian, J. A Review of Remote Sensing for Mangrove Forests: 1956–2018. Remote Sens. Environ. 2019, 231, 111223, doi:10.1016/j.rse.2019.111223.
13. Cavender-Bares, J.; Schneider, F.D.; Santos, M.J.; Armstrong, A.; Carnaval, A.; Dahlin, K.M.; Fatoyinbo, L.; Hurtt, G.C.; Schimel, D.; Townsend, P.A.; et al. Integrating Remote Sensing with Ecology and Evolution to Advance Biodiversity Conservation. Nat. Ecol. Evol. 2022, 6, 506–519, doi:10.1038/s41559-022-01702-5.
14. Sepuru, T.K.; Dube, T. An Appraisal on the Progress of Remote Sensing Applications in Soil Erosion Mapping and Monitoring. Remote Sens. Appl. Soc. Environ. 2018, 9, 1–9, doi:10.1016/j.rsase.2017.10.005.
15. Zhang, X. Reconstruction of a Complete Global Time Series of Daily Vegetation Index Trajectory from Long-Term AVHRR Data. Remote Sens. Environ. 2015, 156, 457–472, doi:10.1016/j.rse.2014.10.012.
16. Tan, B.; Morisette, J.T.; Wolfe, R.E.; Gao, F.; Ederer, G.A.; Nightingale, J.; Pedelty, J.A. An Enhanced TIMESAT Algorithm for Estimating Vegetation Phenology Metrics From MODIS Data. IEEE J. Sel. Top. Appl. Earth Obs. Remote Sens. 2011, 4, 361–371, doi:10.1109/JSTARS.2010.2075916.

17. Li, S.; Xu, L.; Jing, Y.; Yin, H.; Li, X.; Guan, X. High-Quality Vegetation Index Product Generation: A Review of NDVI Time Series Reconstruction Techniques. Int. J. Appl. Earth Obs. Geoinf. 2021, 105, 102640, doi:10.1016/j.jag.2021.102640.
18. Walther, G.-R.; Post, E.; Convey, P.; Menzel, A.; Parmesan, C.; Beebee, T.J.C.; Fromentin, J.-M.; Hoegh-Guldberg, O.; Bairlein, F. Ecological Responses to Recent Climate Change. Nature 2002, 416, 389–395, doi:10.1038/416389a.
19. Kelly, A.E.; Goulden, M.L. Rapid Shifts in Plant Distribution with Recent Climate Change. Proc. Natl. Acad. Sci. 2008, 105, 11823–11826, doi:10.1073/pnas.0802891105.
20. Reichstein, M.; Bahn, M.; Ciais, P.; Frank, D.; Mahecha, M.D.; Seneviratne, S.I.; Zscheischler, J.; Beer, C.; Buchmann, N.; Frank, D.C.; et al. Climate Extremes and the Carbon Cycle. Nature 2013, 500, 287–295, doi:10.1038/nature12350.
21. Zhou, L.; Tian, Y.; Myneni, R.B.; Ciais, P.; Saatchi, S.; Liu, Y.Y.; Piao, S.; Chen, H.; Vermote, E.F.; Song, C.; et al. Widespread Decline of Congo Rainforest Greenness in the Past Decade. Nature 2014, 509, 86–90, doi:10.1038/nature13265.
22. Wu, D.; Zhao, X.; Liang, S.; Zhou, T.; Huang, K.; Tang, B.; Zhao, W. Time-Lag Effects of Global Vegetation Responses to Climate Change. Glob. Chang. Biol. 2015, 21, 3520–3531, doi:10.1111/gcb.12945.
23. Li, J.; Roy, D. A Global Analysis of Sentinel-2A, Sentinel-2B and Landsat-8 Data Revisit Intervals and Implications for Terrestrial Monitoring. Remote Sens. 2017, 9, 902, doi:10.3390/rs9090902.
24. Senf, C.; Leitão, P.J.; Pflugmacher, D.; van der Linden, S.; Hostert, P. Mapping Land Cover in Complex Mediterranean Landscapes Using Landsat: Improved Classification Accuracies from Integrating Multi-Seasonal and Synthetic Imagery. Remote Sens. Environ. 2015, 156, 527–536, doi:10.1016/j.rse.2014.10.018.
25. Adrian, R.; Gerten, D.; Huber, V.; Wagner, C.; Schmidt, S.R. Windows of Change: Temporal Scale of Analysis Is Decisive to Detect Ecosystem Responses to Climate Change. Mar. Biol. 2012, 159, 2533–2542, doi:10.1007/s00227-012-1938-1.
26. Vafeidis, A.T.; Abdulla, A.A.; Bondeau, A.; Brotons, L.; Ludwig, R. Managing Future Risks and Building Socioecological Resilience. Climate and Environmental Hange in the Mediterranean Basin – Current Situation and Risks for the Future; 2021; ISBN hal-03198766f.
27. 24. Appiagyei, B.D.; Belhoucine-Guezouli, L.; Bessah, E.; Morsli, B.; Fernandes, P.A.M. A Review on Climate Change Impacts on Forest Ecosystem Services in the Mediterranean Basin. J. Landsc. Ecol. 2022, 15, 1–26, doi:10.2478/jlecol-2022-0001.
28. 2Noce, S.; Santini, M. Mediterranean Forest Ecosystem Services and Their Vulnerability; 2018;
29. Falanga Bolognesi, S.; Pasolli, E.; Belfiore, O.; De Michele, C.; D'Urso, G. Harmonized Landsat 8 and Sentinel-2 Time Series Data to Detect Irrigated Areas: An Application in Southern Italy. Remote Sens. 2020, 12, 1275, doi:10.3390/rs12081275.
30. Mourad, R.; Jaafar, H.; Anderson, M.; Gao, F. Assessment of Leaf Area Index Models Using Harmonized Landsat and Sentinel-2 Surface Reflectance Data over a Semi-Arid Irrigated Landscape. Remote Sens. 2020, 12, 3121, doi:10.3390/rs12193121.
31. Sousa, D.; Davis, F.W. Scalable Mapping and Monitoring of Mediterranean-Climate Oak Landscapes with Temporal Mixture Models. Remote Sens. Environ. 2020, 247, 111937, doi:10.1016/j.rse.2020.111937.
32. Nguyen, M.; Baez-Villanueva, O.; Bui, D.; Nguyen, P.; Ribbe, L. Harmonization of Landsat and Sentinel 2 for Crop Monitoring in Drought Prone Areas: Case Studies of Ninh Thuan (Vietnam) and Bekaa (Lebanon). Remote Sens. 2020, 12, 281, doi:10.3390/rs12020281.
33. Padró, J.-C.; Pons, X.; Aragonés, D.; Díaz-Delgado, R.; García, D.; Bustamante, J.; Pesquer, L.; Domingo-Marimon, C.; González-Guerrero, Ò.; Cristóbal, J.; et al. Radiometric Correction of Simultaneously Acquired Landsat-7/Landsat-8 and Sentinel-2A Imagery Using Pseudoinvariant Areas (PIA): Contributing to the Landsat Time Series Legacy. Remote Sens. 2017, 9, 1319, doi:10.3390/rs9121319.
34. Chastain, R.; Housman, I.; Goldstein, J.; Finco, M.; Tenneson, K. Empirical Cross Sensor Comparison of Sentinel-2A and 2B MSI, Landsat-8 OLI, and Landsat-7 ETM+ Top of Atmosphere Spectral Characteristics over the Conterminous United States. Remote Sens. Environ. 2019, 221, 274–285, doi:10.1016/j.rse.2018.11.012.
35. Claverie, M.; Ju, J.; Masek, J.G.; Dungan, J.L.; Vermote, E.F.; Roger, J.-C.; Skakun, S. V.; Justice, C. The Harmonized Landsat and Sentinel-2 Surface Reflectance Data Set. Remote Sens. Environ. 2018, 219, 145–161, doi:10.1016/j.rse.2018.09.002.
36. Gouveia, C.M.; Trigo, R.M.; Beguería, S.; Vicente-Serrano, S.M. Drought Impacts on Vegetation Activity in the Mediterranean Region: An Assessment Using Remote Sensing Data and Multi-Scale Drought Indicators. Glob. Planet. Change 2017, 151, 15–27, doi:10.1016/j.gloplacha.2016.06.011.
37. Kottek, M.; Grieser, J.; Beck, C.; Rudolf, B.; Rubel, F. World Map of the Köppen-Geiger Climate Classification Updated. Meteorol. Zeitschrift 2006, 15, 259–263, doi:10.1127/0941-2948/2006/0130.

38. Keeley, J.E.; Bond, W.J.; Bradstock, R.A.; Pausas, J.G.; Rundel, P.W. Fire in Mediterranean Ecosystems: Ecology, Evolution and Management; Press., C.U., Ed.; 2011;
39. Tavşanoğlu, Ç.; Pausas, J.G. A Functional Trait Database for Mediterranean Basin Plants. Sci. Data 2018, 5, 180135, doi:10.1038/sdata.2018.135.
40. Sirami, C.; Nespoulous, A.; Cheylan, J.-P.; Marty, P.; Hvenegaard, G.T.; Geniez, P.; Schatz, B.; Martin, J.-L. Long-Term Anthropogenic and Ecological Dynamics of a Mediterranean Landscape: Impacts on Multiple Taxa. Landsc. Urban Plan. 2010, 96, 214–223, doi:10.1016/j.landurbplan.2010.03.007.
41. Goward, S.N.; Masek, J.G.; Williams, D.L.; Irons, J.R.; Thompson, R.J. The Landsat 7 Mission. Remote Sens. Environ. 2001, 78, 3–12, doi:10.1016/S0034-4257(01)00262-0.
42. Roy, D.P.; Kovalskyy, V.; Zhang, H.K.; Vermote, E.F.; Yan, L.; Kumar, S.S.; Egorov, A. Characterization of Landsat-7 to Landsat-8 Reflective Wavelength and Normalized Difference Vegetation Index Continuity. Remote Sens. Environ. 2016, 185, 57–70, doi:10.1016/j.rse.2015.12.024.
43. Gorelick, N.; Hancher, M.; Dixon, M.; Ilyushchenko, S.; Thau, D.; Moore, R. Google Earth Engine: Planetary-Scale Geospatial Analysis for Everyone. Remote Sens. Environ. 2017, 202, 18–27, doi:10.1016/j.rse.2017.06.031.
44. Claverie, M.; Vermote, E.F.; Franch, B.; Masek, J.G. Evaluation of the Landsat-5 TM and Landsat-7 ETM+ Surface Reflectance Products. Remote Sens. Environ. 2015, 169, 390–403, doi:10.1016/j.rse.2015.08.030.
45. Irons, J.R.; Dwyer, J.L.; Barsi, J.A. The next Landsat Satellite: The Landsat Data Continuity Mission. Remote Sens. Environ. 2012, 122, 11–21, doi:10.1016/j.rse.2011.08.026.
46. Roy, D.P.; Wulder, M.A.; Loveland, T.R.; C.E., W.; Allen, R.G.; Anderson, M.C.; Helder, D.; Irons, J.R.; Johnson, D.M.; Kennedy, R.; et al. Landsat-8: Science and Product Vision for Terrestrial Global Change Research. Remote Sens. Environ. 2014, 145, 154–172, doi:10.1016/j.rse.2014.02.001.
47. Vermote, E.; Justice, C.; Claverie, M.; Franch, B. Preliminary Analysis of the Performance of the Landsat 8/OLI Land Surface Reflectance Product. Remote Sens. Environ. 2016, 185, 46–56, doi:10.1016/j.rse.2016.04.008.
48. Holden, C.E.; Woodcock, C.E. An Analysis of Landsat 7 and Landsat 8 Underflight Data and the Implications for Time Series Investigations. Remote Sens. Environ. 2016, 185, 16–36, doi:10.1016/j.rse.2016.02.052.
49. Drusch, M.; Del Bello, U.; Carlier, S.; Colin, O.; Fernandez, V.; Gascon, F.; Hoersch, B.; Isola, C.; Laberinti, P.; Martimort, P.; et al. Sentinel-2: ESA's Optical High-Resolution Mission for GMES Operational Services. Remote Sens. Environ. 2012, 120, 25–36, doi:10.1016/j.rse.2011.11.026.
50. Louis, J.; Pflug, B.; Main-Knorn, M.; Debaecker, V.; Mueller-Wilm, U.; Iannone, R.Q.; Giuseppe Cadau, E.; Boccia, V.; Gascon, F. Sentinel-2 Global Surface Reflectance Level-2a Product Generated with Sen2Cor. In Proceedings of the IGARSS 2019 - 2019 IEEE International Geoscience and Remote Sensing Symposium; IEEE, July 2019; pp. 8522–8525.
51. Sola, I.; García-Martín, A.; Sandonís-Pozo, L.; Álvarez-Mozos, J.; Pérez-Cabello, F.; González-Audícana, M.; Montorio Llovería, R. Assessment of Atmospheric Correction Methods for Sentinel-2 Images in Mediterranean Landscapes. Int. J. Appl. Earth Obs. Geoinf. 2018, 73, 63–76, doi:10.1016/j.jag.2018.05.020.
52. Louis, J.; Debaecker, V.; Bringfried, P.; Magdalena, M.-K.; Jakub, B.; Mueller-Wilm, U.; Cadau, E.; Gascon, F. Sentinel-2 Sen2Cor: L2A Processor for Users. In Proceedings Living Planet Symposium 2016; Spacebooks Online: Prague, 2016; pp. 1–8 ISBN 978-92-9221-305-3.
53. Zhang, H.K.; Roy, D.P.; Yan, L.; Li, Z.; Huang, H.; Vermote, E.; Skakun, S.; Roger, J.-C. Characterization of Sentinel-2A and Landsat-8 Top of Atmosphere, Surface, and Nadir BRDF Adjusted Reflectance and NDVI Differences. Remote Sens. Environ. 2018, 215, 482–494, doi:10.1016/j.rse.2018.04.031.
54. Zhu, Z.; Woodcock, C.E. Object-Based Cloud and Cloud Shadow Detection in Landsat Imagery. Remote Sens. Environ. 2012, 118, 83–94, doi:10.1016/j.rse.2011.10.028.
55. Foga, S.; Scaramuzza, P.L.; Guo, S.; Zhu, Z.; Dilley, R.D.; Beckmann, T.; Schmidt, G.L.; Dwyer, J.L.; Joseph Hughes, M.; Laue, B. Cloud Detection Algorithm Comparison and Validation for Operational Landsat Data Products. Remote Sens. Environ. 2017, 194, 379–390, doi:10.1016/j.rse.2017.03.026.
56. Flood, N. Comparing Sentinel-2A and Landsat 7 and 8 Using Surface Reflectance over Australia. Remote Sens. 2017, 9, 659, doi:10.3390/rs9070659.
57. Legendre, P.; Legendre, L. Numerical Ecology; 2nd Englis.; Elsevier Science BV: Amsterdam, 1998;
58. Mandanici, E.; Bitelli, G. Preliminary Comparison of Sentinel-2 and Landsat 8 Imagery for a Combined Use. Remote Sens. 2016, 8, 1014, doi:10.3390/rs8121014.
59. Cao, H.; Han, L.; Li, L. Harmonizing Surface Reflectance between Landsat-7 ETM + , Landsat-8 OLI, and Sentinel-2 MSI over China. Environ. Sci. Pollut. Res. 2022, 29, 70882–70898, doi:10.1007/s11356-022-20771-4.

60. K C, M.; Leigh, L.; Pinto, C.T.; Kaewmanee, M. Method of Validating Satellite Surface Reflectance Product Using Empirical Line Method. Remote Sens. 2023, 15, 2240, doi:10.3390/rs15092240.